MultiDIC: a MATLAB Toolbox for Multi-View 3D Digital Image Correlation with Specific In-vivo Biomedical Applications

Dana Solav[1], Kevin M. Moerman[1], Aaron M. Jaeger[1], Katia Genovese[2], Hugh M. Herr[1]

[1] Center for Extreme Bionics, Massachusetts Institute of Technology, Cambridge, MA 02139, USA
[2] School of Engineering, University of Basilicata, Potenza 85100, Italy

ABSTRACT

Three-dimensional Digital Image Correlation (3D-DIC) is an important technique for evaluating the mechanical behavior of materials, including biological tissues. Previous works have improved the performance of computational algorithms, and various commercial and academic 3D-DIC software now exist. Nevertheless, there field lacks 3D-DIC packages which offer straight-forward calibration and data-merging solutions for multi-view analysis, which is particularly desirable in biomedical applications. This paper presents MultiDIC: a 3D-DIC MATLAB toolbox, developed specifically to address this need. MultiDIC is open source and easily adaptable to different experimental settings. MultiDIC integrates the two-dimensional subset-based DIC software Ncorr with a specially developed calibration procedure able to reconstruct 3D points from multiple stereo-pairs. Moreover, it contains algorithms for automatically merging multiple meshes, and for computing and plotting shape, motion, deformation and strain maps. User interfaces allow users to perform 3D-DIC analyses without interacting with MATLAB syntax, while proficient MATLAB users can also use stand-alone functions to write custom scripts for specific experimental requirements. The challenges underlying multi-view DIC are discussed, and the proposed solution is detailed. MultiDIC's performance is demonstrated on experimental data acquired using a low-cost 360° twelve-camera setup. Results of several validation tests, and of in-vivo measurements on a human lower leg are reported.

Keywords

Multi-view Digital Image Correlation; Full-field 3D Deformation; Soft Tissue Biomechanics; Skin Shape; Strain field; Open Source Software;

INTRODUCTION

Digital Image Correlation (DIC) is a full-field non-contact optical-numerical technique to measure shape, motion and deformation, on almost any kind of material, even in extreme experimental settings, as long as the region of interest (ROI) on the sample's surface is provided with a natural or synthetic speckle pattern[32,47]. This allows the DIC algorithm to match dense sets of corresponding points in different images of the ROI, based on the local pixel intensity distribution. Specifically, local 2D-DIC[32] defines a pixel subset around a point of interest in a reference image and evaluates the parameters describing its motion and deformation in a given target image. In 3D-DIC, two cameras view an ROI from different angles (i.e. a stereo-camera pair), and capture a sequence of images representing a reference configuration (typically an undeformed configuration) and a required number of "current" configurations (typically deformed configurations). Next, 2D-DIC is used to correlate a given set of points in the two stereo-views of the reference configuration (spatial correlation) and track these points throughout the sequence of stereo-images representing the current configurations (temporal correlation). The correlated sets of image points are then used to reconstruct and track the 3D position of the material points of the ROI over time, via stereo-triangulation[11,47].

DIC was originally developed for experimental mechanics, where it has become a standard technique for characterizing material properties and the response of structures to loads[17]. The non-contact, full-field, and large deformation capabilities of DIC make it particularly suited for shape and deformation measurements for a wide range of biomedical applications[2,3,7,13,19,22,30]. DIC methods have been used in combination with advanced inverse characterization methods to identify the mechanical properties of natural and synthetic biological materials and body parts[2,3,13,30].

Substantial work has been done in recent decades to improve the performance of computational algorithms[12,15,33,34,46,52], to define good practices for performing experiments and calibration[38], to assess the measurement errors[20,51], and to extend the capabilities of 3D-DIC[45,46]. Furthermore, various commercial and academic software packages now exist. However, there is currently a lack of available 3D-DIC software specifically tailored for multi-view analysis, a feature which is highly desirable for biomedical applications. It is challenging to study the shape, motion, and deformation of tissues and organs in-vivo, due to the often complex geometries, the large deformations that can occur, and the risk undesired motions. These challenges often require simultaneous multi-view imaging[19,28]. Moreover, in a clinical environment, a fast and flexible image acquisition and calibration process is highly desirable[18].

Several multi-view DIC systems have been proposed in literature[8,14,23,28,29,50], where multiple cameras with partially overlapping fields of view (FOVs) allow for the imaging of large portions of an object surface. The multitude of cameras can be arranged in a 2D-array when large quasi-planar objects need to be measured. Alternatively, for non-planar objects, the set of cameras are placed around the object, e.g. in a surrounding fashion, to obtain the 3D shape of the entire object (as illustrated in Fig. 1). In this work, we refer to the latter configuration, which is suitable for many biomedical applications.

Furthermore, in scientific research reproducibility, verifiability, and validation are key[9]. Only open source software tools offer full insight into the computational framework these aspects demand. Furthermore, open source software enables customizability, which is important since

each scientific application offers its own unique computational and experimental challenges. There is hence a pressing need for open source software implementing algorithms specifically tailored for multi-view 3D-DIC, which allow for customization and easy adaptation to different experimental settings.

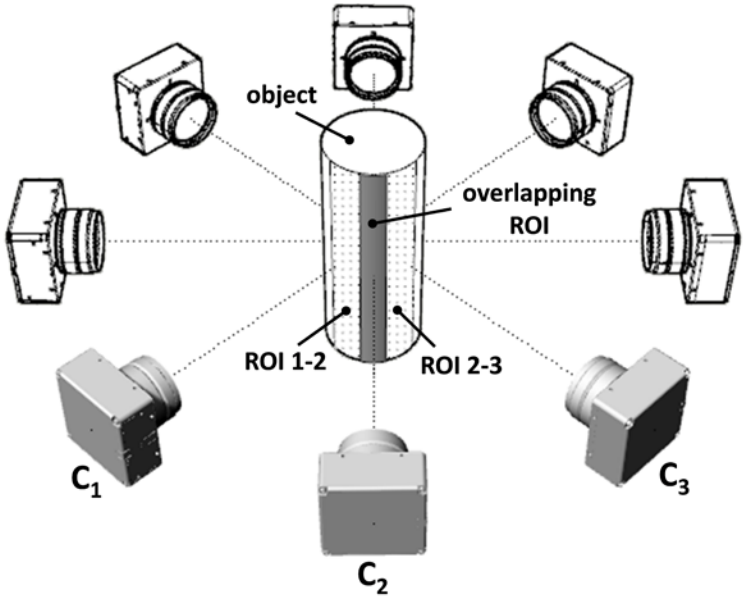

Fig. 1. Schematic of a multi-view system showing a circular array of cameras (in transparent color) surrounding the object, with highlighted two contiguous stereo-pairs (in solid color), sharing a common field of view on the object's surface. The ROI for each pair is depicted on the object's surfaces with dots, and the overlapping ROI for the two pairs is depicted with solid color.

Theoretical Background

Two key issues entailed in the implementation of multi-view setups are system calibration (required for stereo-triangulation) and data merging (required for combining results from multiple stereo-pairs). For each camera of a typical stereo-pair, calibration aims to find the intrinsic parameters (defining the geometric and optical characteristics of the camera) and the extrinsic parameters (defining the position and orientation of the camera with respect to a reference coordinate system). Together, the intrinsic and extrinsic parameters serve to describe the transformation that maps each 3D material point $\boldsymbol{P}(X,Y,Z)$ in the global coordinate system into its image point on the camera sensor $I(x_P,y_P)$, according to the pinhole optical model[1,11]. Specifically, the coordinates of $\boldsymbol{P}(X,Y,Z)$ are first rigidly transformed into the coordinates (X_C,Y_C,Z_C) in the camera coordinate system by

$$\begin{bmatrix} X_C \\ Y_C \\ Z_C \end{bmatrix} = \begin{bmatrix} R_{11} & R_{12} & R_{13} \\ R_{21} & R_{22} & R_{23} \\ R_{31} & R_{32} & R_{33} \end{bmatrix} \begin{bmatrix} X \\ Y \\ Z \end{bmatrix} + \begin{bmatrix} T_X \\ T_Y \\ T_Z \end{bmatrix}, \tag{1}$$

where R_{ij} $(i,j = 1,2,3)$ and T_x, T_y, T_z are the components of the rotation matrix and the translation vector, respectively. Next, the (ideal) normalized image point coordinates are calculated as

$$x = \frac{X_C}{Z_C} \; ; \quad y = \frac{Y_C}{Z_C} \; . \tag{2}$$

Then, the intrinsic camera parameters, i.e. the focal lengths in pixels$\left[f_x, f_y\right]$, the principal point (optical center) coordinates $\left[C_x, C_y\right]$, and the skew coefficient $s = f_y \tan\alpha$, where α is the angle between the horizontal and vertical axes of the sensor ($\alpha = s = 0$ if the axes are perpendicular), are used to calculate the image point coordinates $I(x_P, y_P)$, in the sensor reference system by

$$\begin{bmatrix} x_p \\ y_p \\ 1 \end{bmatrix} = \begin{bmatrix} f_x & s & C_x \\ 0 & f_y & C_y \\ 0 & 0 & 1 \end{bmatrix} \begin{bmatrix} x \\ y \\ 1 \end{bmatrix}. \tag{3}$$

Next, combining equations (1)-(3) and further assuming that $s = 0$ yields to

$$x_p = f_x \frac{R_{11}X + R_{12}Y + R_{13}Z + T_x}{R_{31}X + R_{32}Y + R_{33}Z + T_z} + C_x \tag{4a}$$

$$y_p = f_y \frac{R_{21}X + R_{22}Y + R_{23}Z + T_y}{R_{31}X + R_{32}Y + R_{33}Z + T_z} + C_y, \tag{4b}$$

which can be rearranged into the form

$$x_p = \frac{L_1X + L_2Y + L_3Z + L_4}{L_9X + L_{10}Y + L_{11}Z + 1} \tag{5a}$$

$$y_p = \frac{L_5X + L_6Y + L_7Z + L_8}{L_9X + L_{10}Y + L_{11}Z + 1}. \tag{5b}$$

Eq. (5) represents the basis of the Direct Linear Transformation (DLT) method[1] which allows for implicit camera calibration. The DLT method derives (unphysical) parameter set L_j $(j = 1, 2, \dots, 11)$ by solving a linear system of equations, based on a *single* image containing a non-planar set of calibration points whose positions (X, Y, Z) are known with high accuracy. DLT, however, relies on an idealized distortion-free camera model which might yield inaccurate results, especially when high-distortion or low-quality lenses are used.

The most common stereo calibration technique used in 3D-DIC methods is the Bundle Adjustment (BA) method [47]. BA is an explicit calibration method that allows for the estimation of both the intrinsic and extrinsic camera parameters by using repetitive observations of sparse scene points in different viewing directions[48]. BA allows for lens distortion correction (DC) based on a non-linear distortion model. Specifically, the idealized image point coordinates (x, y) in Eq. (3), are replaced by the distorted normalized coordinates (x_d, y_d) defined by

$$\begin{bmatrix} x_d \\ y_d \end{bmatrix} = (1 + k_1 r^2 + k_2 r^4 + k_3 r^6) \begin{bmatrix} x \\ y \end{bmatrix} + \begin{bmatrix} 2p_1 xy + p_2(r^2 + 2x^2) \\ p_1(r^2 + 2y^2) + 2p_2 xy \end{bmatrix}, \quad (6)$$

where $r^2 = x^2 + y^2$, $[k_1, k_2, k_3]$ are the radial distortion parameters, $[p_1, p_2]$ are the tangential distortion parameters, and the skew parameter in Eq. (3) can be non-zero.

Successful BA typically requires a *large number* of images (approximately 50[37]) of a planar calibration target acquired in different orientations and positions in the field of view (FOV) of both cameras. Although BA is highly accurate, and is typically the first choice for calibrating a two-camera system, the associated practice of calibrating one camera with respect to a given 'master' camera can limit its applicability to multi-view stereo systems. To calibrate a large number of camera-pairs, each camera-pair has to be calibrated separately. Then, the images of a given set of markers[23], or of a speckled surface[6], which can be viewed by each contiguous pair of cameras, are used to: 1) find the geometric transform between the pairs, and 2) combine the data into a mutual coordinate system[6]. This process has to then be repeated for each additional camera-pair[6]. Clearly, this approach is very time-consuming, especially in case a large number of cameras is required or when the camera poses change during a data collection session, potentially causing error accumulation. Furthermore, this method does not enable combining data from camera-pairs for which the fields of view do not overlap.

In contrast, the DLT method can use a single image acquisition of a 3D calibration target placed in the scene, captured by all the cameras of the multi-view system. This arrangement allows one to calibrate each camera with respect to a common reference system associated to the 3D target, thus enabling an automatic data merging. The main limitation of this approach is that the calibration target usually covers only a portion of the capture volume and this may affect the accuracy of the calibration results, even when DC procedures are adopted[16].

Overview of the current work

A specific aim of this work was to overcome the above-mentioned limitations of existing multi-view methods. To this end, we present MultiDIC, a free open source software library for analyzing multi-view stereo images and obtaining 3D shapes and full-field displacements, deformations, and strains. Specific consideration is given to develop a procedure for simple multi-view stereo calibration and data merging, which enables the camera pose to be changed as needed, without requiring a long re-calibration process. MultiDIC integrates the high-quality open source 2D-DIC software Ncorr[5], which was previously verified and validated by analyzing standard sets of synthetic and experimental images[38]. In the present study, a combined approach was developed, whereby both BA and DLT are used in different steps, to harness the advantages of each method. Particularly, BA is used for obtaining the distortion and skew parameters, which can be used to undistort both the stereo calibration images and the speckled images. BA is only needed once per camera, as long as the camera's internal settings remain unaltered. DLT is then used on the undistorted image points for retrieving the internal (distortion-free) and external (camera pose) parameters of the cameras, combined into the DLT parameters. The DLT parameters refer to a common global coordinate system associated with the 3D calibration target seen simultaneously from all the cameras. Since only a single image per camera is required, DLT can also be used also to check the stability of the system whenever experiments are prolonged in time, and to quickly re-calibrate they system in case cameras are intentionally or accidentally moved. Moreover, this

rationale allows one to eventually keep the original images and skip the distortion correction step in cases where images are obtained with high quality optics and sensors[14], or if the distortions are known to be negligible with respect to the required precision for the specific application.

When a large number of views is required, as is often the case of biomedical applications, imaging systems can become prohibitively expensive. In this study, we present an inexpensive system using low-cost camera modules with which we test the capabilities of the toolbox. This paper describes the workflow of the software and the algorithms implemented in it, the experimental setups, and the data analysis procedures. Then, results of several tests that both validate it and showcase its capabilities are reported and discussed. Finally, testing with a human lower limb demonstrates the typical shape and deformation information obtainable for in-vivo studies.

MATERIALS AND METHODS

Overview of Software Architecture and Algorithms

The MultiDIC is an open source (Apache 2.0 licensed) library written in the MATLAB (The Mathworks Inc., USA) programming language, a language widely used among engineers and scientists. Users may visit the GitHub repository (http://www.github.com/MultiDIC) to obtain the most recent version, to join development, and to post issues. The toolbox is accompanied by a comprehensive instruction manual and sample data.

MultiDIC was designed as a flexible library of functions and scripts that users can freely adjust to fit their experimental requirements. The implementation as a toolbox enables users to perform 3D-DIC analyses and to plot results based on user interfaces, which do not require interaction with MATLAB syntax. As such, these interfaces provide access to the most common functionality as well as usability for non-code experts. For customization, proficient MATLAB users can also use the stand-alone functions and data-structures to write custom scripts and analyze large data-sets semi-automatically. Moreover, users are encouraged to extend the toolbox's functionality by implementing additional algorithms.

MultiDIC integrates the 2D-DIC software Ncorr[5] with the BA algorithm implemented in the MATLAB computer vision toolbox[54], and the DLT algorithm, to perform the reconstruction of 3D surfaces from multiple stereo-image pairs. Moreover, it contains algorithms for merging surfaces, and for computing 3D displacements, deformations, strains, and rigid-body motion (RBM). In addition, extensive plotting and visualization functions are offered, which integrate tools from the open source GIBBON toolbox[24].

Fig. 2 outlines the workflow of the entire 3D-DIC procedure. In the optional step 0, the distortion and skew parameters are calculated using BA on multiple images of a flat checkerboard. These parameters can be used to correct for the effect of distortion on the points detected on both the calibration object images and the speckled object images. Step 1 comprises the calculation of the DLT calibration parameters of each camera, using images of a 3D calibration object seen simultaneously from all the views. Step 2 involves matching corresponding points on sets of stereo images of the speckled object using 2D-DIC. In step 3, the calibration parameters from step 1 are used to perform a stereo-triangulation which transforms the 2D points matched in step 2 for each stereo-pair into 3D triangular meshes. Furthermore, this step may optionally

involve the merging together of multiple obtained surfaces. Lastly, step 4 includes algorithms for computation and visualization of displacements, deformations, strains, and RBM. The methods implemented in each of these steps are detailed in the next sub-sections.

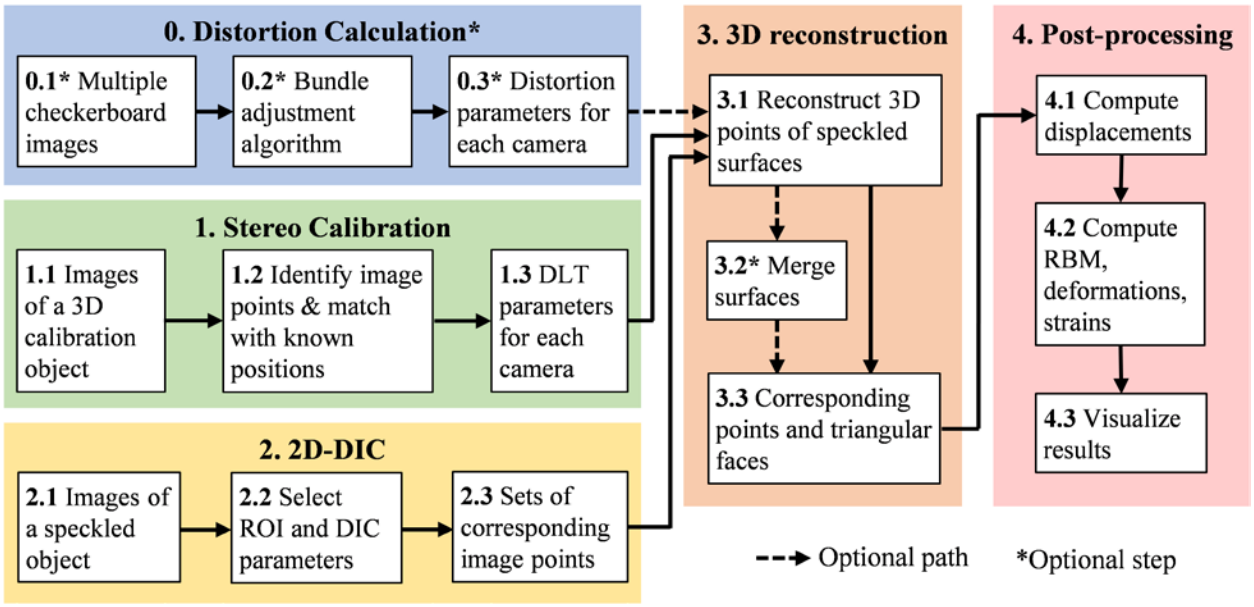

Fig. 2. The workflow of the 3D-DIC algorithms implemented in MultiDIC. Step 0 is optional, and is only required if distortion correction is necessary. Step 1 and 2 and 3 comprise the core components of the 3D-DIC process. Moreover, step 3.2 is optional, and is only required if merging of surfaces into one continuous mesh is desired.

Distortion Correction

The purpose of this step is to find the parameters for correcting the lens distortions and skew affecting the acquired images. This step has to be executed only once per camera and needs not be repeated if a camera pose is changed, as long as the camera's intrinsic parameters remains unaltered. The MATLAB Camera Calibration Toolbox[54] was utilized for evaluating the camera intrinsic parameters, including distortion parameters using the BA method. Multiple images of a planar checkerboard pattern are acquired by each camera. Then, the algorithm utilizes BA to minimize the overall re-projection errors of the checkerboard pattern's corner points. The implemented model allows for the computation of up to six parameters: three for radial distortion, two for tangential distortion, and one for skew, as detailed in Eq. (3) and Eq. (6). These parameters are later used before 3D reconstruction, to remove the distortion from points detected on both the stereo calibration images and the speckle images.

Stereo Calibration

In this step, the mapping between 2D image points and 3D world points is established, using Eq. (5). Since each control point provides two equations, a minimum of six points is required to obtain the set of DLT parameters L_i. Nevertheless, a greater number of points is preferred, as the effect of experimental errors is reduced by solving an overdetermined system through least-squares minimization.

In practice, this step requires a 3D calibration object having control points whose 3D positions

are known with sufficient accuracy. The use of a 3D object with axial-symmetry (a cylinder in the current study) represents the optimal solution for a 360° multi-view system, since images of the calibration object can be acquired from all cameras simultaneously. The calibration images are then analyzed using MultiDIC to detect the image points (x_P, y_P), and to sort and match them with the known 3D positions (X, Y, Z). Next, the DLT parameters and the associated reconstruction errors are calculated and plotted.

2D-DIC of Stereo Image Pairs

In this step, which is repeated for each camera-pair, corresponding image points are detected on sets of images of a speckled object acquired from two angled views, as illustrated in Fig. 3. First, a reference image is selected, typically the image acquired in the undeformed configuration from either one of the views. Second, a ROI is selected, which corresponds to an area of the object which is visible from both views. Third, a point grid is obtained inside the ROI according to selected subset size and spacing, and corresponding points are detected on all the remaining images of the set using Ncorr[5]. Ncorr is an open source subset-based 2D-DIC software, described in detail in [5] together with validation results of its metrological performances tested with images from the 2D-DIC-Challenge[38]. Briefly, Ncorr implements a first order shape function to describe the pixel subset transformation[32], the least-square correlation criterion C_{LS} as a correlation cost function[5], the Inverse Compositional Gauss-Newton method as a nonlinear optimizer[4], and the Reliability-guided method[31] to propagate the analysis over the ROI, starting from user-defined seed points.

Moreover, a triangular mesh is defined on the point grid and saved for the 3D reconstruction step. Specifically, MultiDIC's step 2 serves as a wrapper for Ncorr, which allows users to select camera-pairs for analysis and draw the ROI. These data are automatically transferred into Ncorr for further analysis, and the corresponding image points, together with the associated correlation coefficients [5] are returned for defining the triangular mesh, for plotting the results, and for saving the variables necessary for 3D reconstruction.

Fig. 3 illustrates how Ncorr was able to obtain high correlation accuracies (low values of C_{LS}) over most of the selected ROI with exception of the right border, where the first order shape function could not correctly describe the curved portion of the surface[21]. In this work, a sufficiently large number of cameras (i.e. narrow ROI for each camera pair) were chosen to ensure high accuracy correlation, even on complex shaped parts.

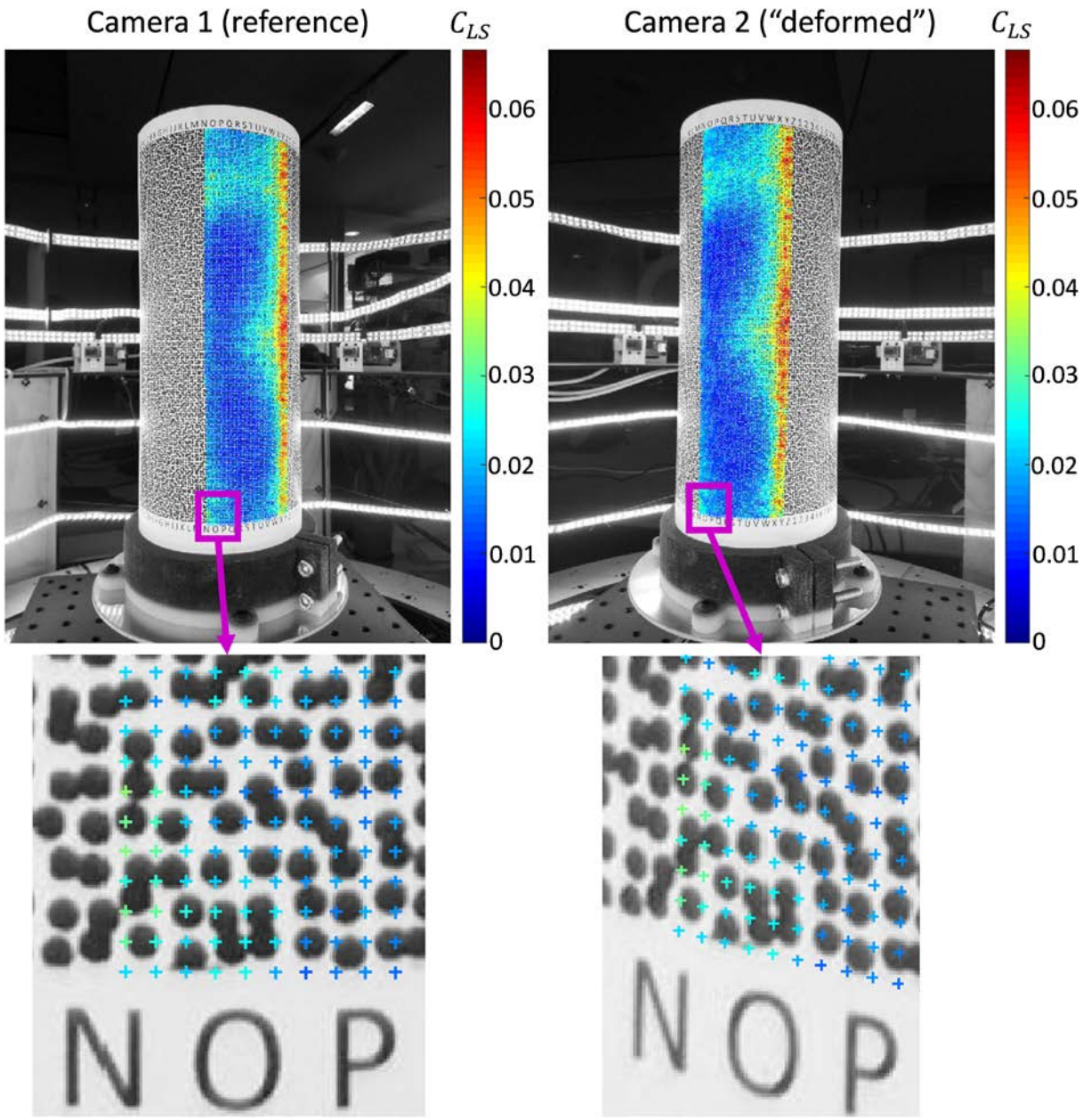

Fig. 3. 2D-DIC point matching between two stereo images. Portions of a speckled cylindrical object imaged by cameras positioned with an angular displacement of 30° between them are shown. The corresponding image points detected using DIC inside the ROI are shown on the reference (left) and "deformed" (right) images, with colors depicting the values of the correlation coefficient.

3D Reconstruction and surface merging

In this step, the DLT parameters $L_j^{C_k}$ $(j = 1, 2, \dots, 11;\ k = 1, 2)$ associated with cameras C_1 and C_2 of each stereo-pair, are used to transform each pair of corresponding image points, from their

image coordinates $\left(x_p^{C_1}, y_p^{C_1}\right)$ and $\left(x_p^{C_2}, y_p^{C_2}\right)$, into the 3D coordinates (X, Y, Z), by rearranging Eq. (5) into the form

$$\boldsymbol{U} = \boldsymbol{A}\boldsymbol{P}\,, \tag{7}$$

where

$$\boldsymbol{U} = \begin{bmatrix} x_p^{C_1} - L_4^{C_1} \\ y_p^{C_1} - L_8^{C_1} \\ x_p^{C_2} - L_4^{C_2} \\ y_p^{C_2} - L_8^{C_2} \end{bmatrix};\quad \boldsymbol{P} = \begin{bmatrix} \mathrm{X} \\ \mathrm{Y} \\ \mathrm{Z} \end{bmatrix};$$

$$\boldsymbol{A} = \begin{bmatrix} L_1^{C_1} - L_9^{C_1} x_p^{C_1} & L_2^{C_1} - L_{10}^{C_1} x_p^{C_1} & L_3^{C_1} - L_{11}^{C_1} x_p^{C_1} \\ L_5^{C_1} - L_9^{C_1} y_p^{C_1} & L_6^{C_1} - L_{10}^{C_1} y_p^{C_1} & L_7^{C_1} - L_{11}^{C_1} y_p^{C_1} \\ L_1^{C_2} - L_9^{C_2} x_p^{C_2} & L_2^{C_2} - L_{10}^{C_2} x_p^{C_2} & L_3^{C_2} - L_{11}^{C_2} x_p^{C_2} \\ L_5^{C_2} - L_9^{C_2} y_p^{C_2} & L_6^{C_2} - L_{10}^{C_2} y_p^{C_2} & L_7^{C_2} - L_{11}^{C_2} y_p^{C_2} \end{bmatrix}. \tag{8}$$

Then, the least-squares solution for $\boldsymbol{P}$ is obtained by

$$\boldsymbol{P} = [\boldsymbol{A}^T\boldsymbol{A}]^{-1}\boldsymbol{A}^T\boldsymbol{U}\,. \tag{9}$$

Consequently, a 3D point cloud is obtained from each stereo-pair. Since the coordinates of the control points on the calibration object, used to obtain the DLT parameters, are expressed in the global coordinate system for all camera-pairs, all point clouds are automatically reconstructed in the global coordinate system, without the need to perform any additional coordinate transformation procedure.

The tessellation defined in step 2 is used here to form sets of 3D triangular meshes. The meshes obtained from each camera pair are independent, not connected to each other, and may locally overlap. In order to construct a single continuous and merged surface, the overlap between meshes needs to be resolved and adjacent meshes should be stitched together. An example schematic for resolving overlap and for merging two adjacent surfaces is shown in Fig. 4.

To resolve the overlap, an algorithm was developed, whereby redundant faces are iteratively removed from the boundaries of overlapping regions until a user-defined minimum gap exists between the meshes. The following heuristics are employed to select which faces to remove:

1. The DIC correlation coefficient, representing the matching quality of each vertex (removing vertices with poorer correlation first).
2. The distance between the meshes in the overlap region (removing faces having larger distance to the other mesh first).
3. The difference in the local orientation between the meshes in the overlap region (removing faces having larger angular displacement from the other mesh first).
4. A combination of 1, 2, and 3, with optional weights.

Once the overlap is resolved (Fig. 4B), the meshes are merged by introducing new faces along the gap, connecting original vertices from both meshes, as depicted in Fig. 4C. The algorithm uses

only vertices which exist in the original data. Introduction of new vertices which do not originate from an actual measurement is not desirable, since these vertices cannot be tracked in the deformed states and cannot provide reliable displacement and strain measurements. Moreover, keeping all the points and re-meshing the overlapping regions is not preferred because it results in a denser and often lower quality mesh, and might result in a jagged surface in regions where the two surfaces could not accurately merge. Stitching of the gap is performed by locally applying Delaunay triangulation between the vertices of the meshes' boundaries, which maximizes the minimum angle of the triangles and ensures that quality triangles are formed.

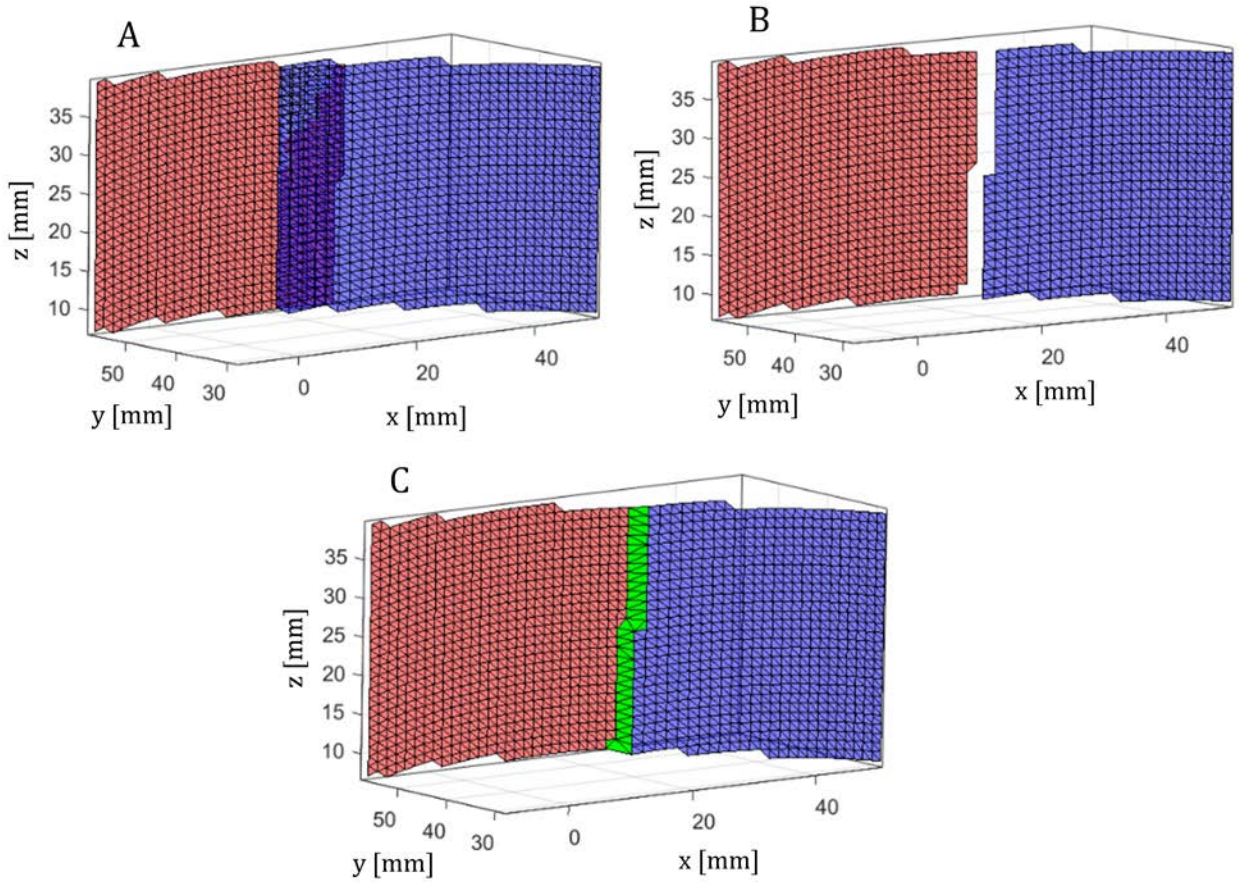

Fig. 4. Surface merging example. (A) The red and blue 3D surfaces were reconstructed from two adjacent camera-pairs. (B) The overlap regions are identified, and faces are removed from the boundaries until the overlap is resolved and a minimum gap exist between the surfaces. (C) The gap is filled with new triangular faces, using only vertices existing in the original data.

Post-processing

In this step, the 3D coordinates of the triangular mesh's vertices in the reference and current configurations are used to derive the deformations and strains, as described in detail in Appendix A.

MultiDIC offers functions for the dynamic visualization of the displacements, stretches and

strains (magnitude and direction), surface area change, as well as additional measures such as the correlation coefficient and the color texture from the original images.

Metrological performance assessment

A 360° stereo camera rig was designed and fabricated, to hold up to 30 cameras (Raspberry Pi Camera Module V2, featuring a Sony IMX219 8-megapixel $3.674 \times 2.760\ \mathrm{mm}^2$ CMOS sensor, connected to Raspberry Pi Zero-w) in a 700 mm diameter circle, as shown in Fig. 5. The objects to be imaged were placed in the center of the circle where it could be uniformly illuminated by circular arrays of flexible LED strips. All cameras were connected and synchronously controlled using an Ethernet hub. For the experiments described in this paper, twelve cameras were placed coaxially, resulting in twelve stereo-pairs having 30° between them, such that the distance between each pair of contiguous cameras is 181.17 mm. This angle is small enough to provide both a sufficient overlapping portion and an acceptable level of distortion between image-pairs, and at the same time large enough to allow for accurate out-of-plane displacement measurements[20,51]. The system was very low-cost (<$1,000 total, including 12 cameras, cables, LEDs, Ethernet hub, and power supplies).

A 3D calibration object was prepared by accurately lathing a 250 mm long, 114 mm diameter aluminum cylinder, to achieve a uniform diameter throughout the cylinder's length. This cylinder was then wrapped in a white adhesive paper with a printed grid pattern of black square dots (4 mm by 4 mm squares, 12 mm spacing), see Fig. 5. To evaluate the errors associated with stereo calibration independently of the DIC process, an experiment was performed, whereby the 3D positions of the calibration object's dots were analyzed before and after a 5 mm displacement was applied with a motorized linear stage (Zaber Technologies A-LSQ075B-E01, max 0.5 μm microstep error), as shown at the bottom of the cylinder in Fig. 5A, and the close-up in Fig. 5D. The reconstructed 3D points were then superimposed into their reference positions by estimating the optimal RBM between them.

The next set of verification experiments involved a 3D speckled test object that was prepared by applying an adhesive paper with a speckle pattern (black 1.4 mm circles printed in a random pattern on white paper) to the aluminum cylinder (see Fig. 3). The cylinder's surface was imaged using the camera rig and analyzed using MultiDIC. The performance of the complete 3D-DIC algorithm and experimental system was evaluated by analyzing the correctness of shape, by the merging errors between adjacent camera-pairs, the displacement errors, and the strains.

The correctness of the shape measurement was evaluated by comparing the fitted diameter of the reconstructed cylinder to the diameter measured using a large-capacity caliper (±0.01 mm accuracy). Next, the merging errors between surfaces reconstructed by different camera-pairs were evaluated by reconstructing a portion of the surface visible by three adjacent cameras (the overlapping region illustrated in Fig. 1). The center camera (C_2) was defined as the reference camera for the two pairs: $[C_2, C_1]$ and $[C_2, C_3]$, such that the same reference point grid was used for both pairs. Next, the cylinder was translated using the motorized linear stage, in 10 steps of 0.1 mm increment, and the displacements errors were calculated by comparing the displacements measured using 3D-DIC and those measured using the stage. Moreover, the 3D strains, which should theoretically equal to zero for RBM, were analyzed to evaluate the overall accuracy of the strain measurement.

Finally, to demonstrate the capability of the proposed methods to measure in-vivo shapes and

deformations, the surface of the lower limb of a human subject was measured. A custom speckling stamp was made by laser-engraving a rubber sheet with same speckle pattern described above. A uniform layer of white temporary tattoo ink (ProAiir, USA) was applied to the skin surface to enhance contrast and to create a homogenous background. Next, the speckle pattern was applied with black temporary tattoo ink (ProAiir, USA) using the stamp. The subject's lower leg was imaged while the subject performed unconstrained ankle dorsi-flexion and plantar-flexion. The experimental procedure was approved by the Committee on the Use of Humans as Experimental Subjects of the Massachusetts Institute of Technology (COUHES protocol: 1101004280).

All the DIC analyses were performed using 20 pixels subset radius and 10 pixels step size at a $\sim 10\ pixel/mm$ ratio. All the results represent raw data. No kind of filtering or smoothing procedures were applied.

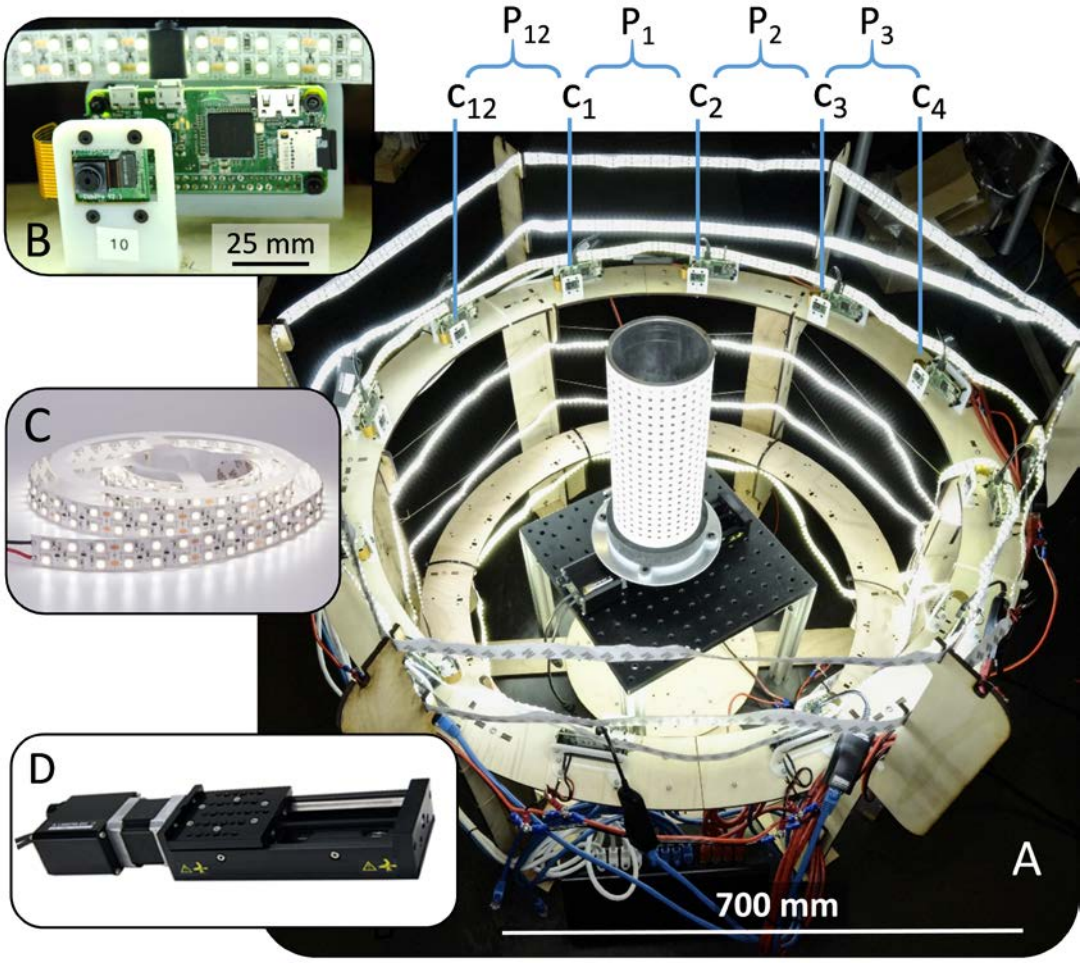

Fig. 5. Experimental setup. (A) The 360° rig holding 12 Raspberry Pi camera units (enlarged inset B). Each pair of adjacent cameras [C_1,C_2], [C_2,C_3]…[C_{12},C_1], constitute a stereo-pair (P_1, P_2 … P_{12}). The calibration object is placed at the center of the rig and illuminated using flexible LED strips (enlarged inset C). A motorized translation stage (enlarged in inset D) was placed under the calibration object for the validation experiments.

RESULTS

The intrinsic parameters calculated for all cameras, as well as the reconstruction errors, are reported in Appendix B.

Stereo calibration test

Fig. 6 reports the stereo calibration errors, represented by the Euclidian distances between corresponding points of the calibration object measured in two positions and rigidly superimposed. Fig. 6A illustrates the error magnitudes of individual points, and Fig. 6B summarizes the statistics of the 3D components of the errors obtained with and without distortion correction. The mean errors were very small both with and without distortion correction ($\sim 10^{-14}$), but the root mean square (RMS) and standard deviation (STD) of the error magnitudes were significantly lower when the distortion correction was employed (0.017 mm) than when it was not employed (0.026 mm).

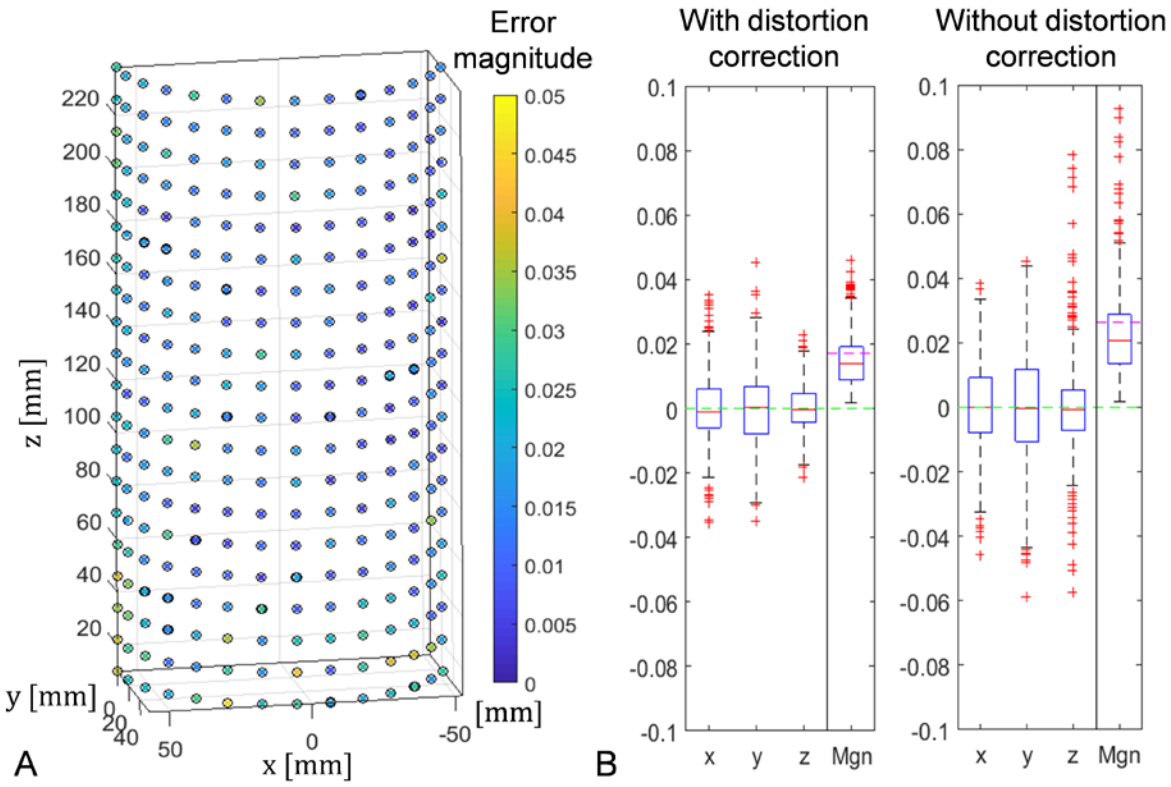

Fig. 6. Stereo calibration errors evaluated by analyzing two sets of calibration object images, before and after 5 mm displacement. (A) The 3D positions of half of the calibration object's dots reconstructed in the first set are plotted as black hollow circles, and the positions from the second (displaced) set superimposed into the first, are plotted with colors depicting the absolute distance between them. (B) The error statistics for all the points, obtained with and without distortion correction, in the x, y, and z directions, and the error magnitude (Mgn). The boxplots report the median (red line), 25th and 75th quartiles (blue box), and outliers (red crosses). The green dashed line represents zero error, and the magenta dashed line represents the root mean square error.

3D-DIC tests of a rigid speckled object

The errors reported in this section are associated with the entire 3D-DIC procedure. The correctness of the shape measurement was evaluated by comparing the fitted diameter of the reconstructed cylinder to the 114.00 mm diameter (including the adhesive paper) measured using the caliper. The mean ± standard deviation of the diameter measured using 3D-DIC was 113.93 ± 0.27 and 113.91 ± 0.56 mm, with and without distortion correction, respectively.

The merging errors between surfaces reconstructed by different camera-pairs are shown in Fig. 7A. The reconstructed points are plotted with colors depicting the magnitude of the Euclidean distance between the two sets. The mean ± standard deviation of the errors were 0.06 ± 0.03 mm and 0.08 ± 0.06 mm, with and without distortion correction, respectively. As expected, the distortion correction improved the merging accuracy mostly in the ROI's upper and lower ends, corresponding to the marginal areas of the images.

The displacements and displacement errors are summarized in Fig. 7B (top and center) as a function of the imposed displacement. Fig. 7C shows the strain magnitude distribution over half of the cylinder, for a displacement of 0.5 mm, and the statistics for all displacement steps are summarized in Fig. 7B (bottom).

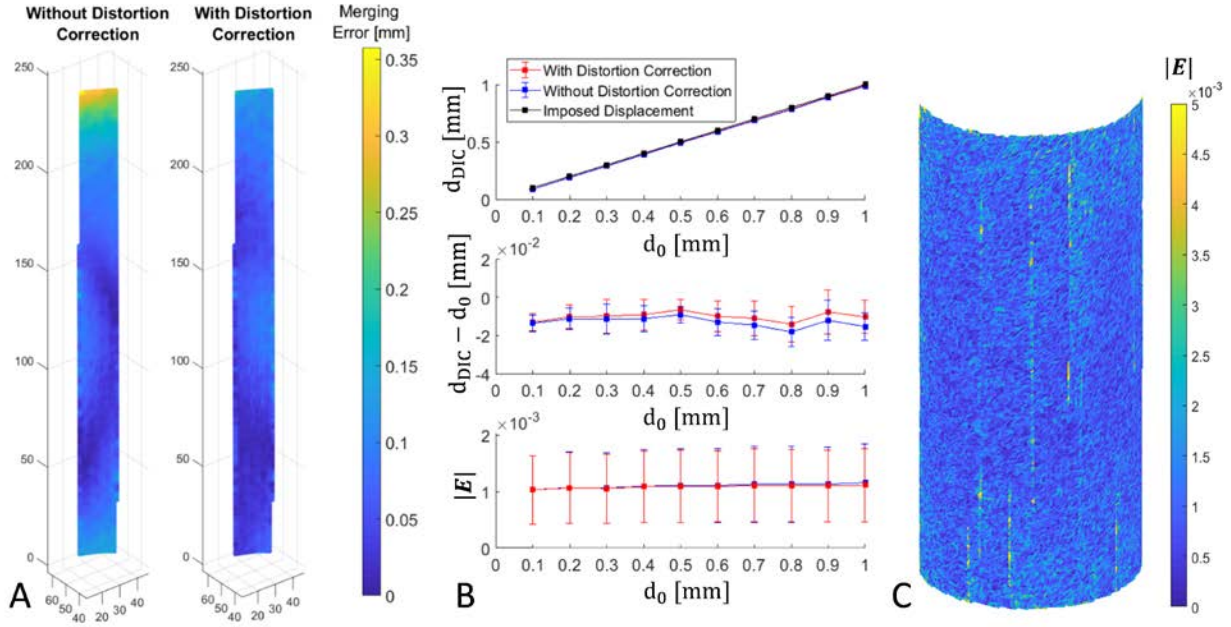

Fig. 7. 3D-DIC results of a rigid speckled cylinder. (A) Merging error depicted as the Euclidian distance between the points reconstructed by two adjacent camera-pairs (overlapping region in Fig. 1); (B) Results from a set of 10 imposed translations (d_0) with a 0.1 mm increment. The measured displacements (top), displacement errors (center) and Green-Lagrangian strain magnitude (bottom) are plotted as error bars which represent ± one standard deviation over all data points; (C) The Green-Lagrangian strain magnitude distribution plotted on half of the cylinder, for the 0.5 mm displacement step.

3D-DIC in-vivo tests of a deformable body segment

Illustrative results from the 3D-DIC in-vivo measurements are shown in Fig. 8. The full surface of the calf region of the lower leg was imaged five times while the subject plantar-flexed. Results of the first and the last frames are illustrated. Images A-D show 2D-DIC results for one stereo-pair. Image A is the reference image, on which the point grid was defined. Images B-D represent deformed states of image A (note that the image distortion with respect to image A is due to perspective in B, due to deformation in C, and to perspective and deformation in D). Fig. 8E-G show the full surface reconstructed by 12 cameras in the reference (E) and deformed (F and G) configurations. The face colors depict the value of the first (F) and second (G) principal stretches, and the black lines represent their directions, with lengths proportional to the stretch magnitude. Since image E shows the reference configuration, the stretch values equal to one by definition. The strain fields are visibly smooth, despite the facts that it was computed independently on each triangular face and that no smoothing or filtering was applied to the raw data, contrarily to common DIC strain calculation schemes[36,47]. Animated figures showing the dynamic values of the displacement magnitude, surface area change, and principal stretches, are provided as electronic supplementary material.

DISCUSSION

This paper describes the principal algorithms implemented in MultiDIC, a newly developed 3D-DIC MATLAB toolbox for multi-camera system with special application to biomedical in-vivo measurement. The methods and system were designed to overcome some of the limitations involved with common calibration and data merging techniques. One primary advantage is that it allows for a simple calibration process even when using a large number of cameras, without losing the ability to compensate for lens distortions. Consequently, the new method offers the flexibility of modifying the camera poses during experiments without requiring substantial additional re-calibration time.

The metrological capabilities of MultiDIC were validated by several experimental tests using a low-cost multi-camera setup. The errors associated with the proposed stereo calibration method were examined independently of the DIC procedure, by analyzing the 3D positions of the calibration object's control points in two configurations. The 3D reconstruction errors when using distortion correction procedure was 0.000 ± 0.017 mm (STD and RMS 35% lower than without distortion correction). These are relatively low considering the large size of the calibration object, and the cameras' large FOV and very low price.

Next, the metrological errors associated to the entire multi-view DIC procedure were evaluated by measuring shape, displacement and strain error with a speckled cylindrical object. The shape measurements revealed errors less than 0.01 mm (<0.1%) in obtaining the cylinder's diameter. The merging errors and displacement errors were also found to be in the order of 0.01 mm, which is comparable to the stereo calibration errors. Furthermore, the strains measured as a result of RBM were in the range of 10^{-3}, which is sufficiently accurate in our case, and is acceptable in most biomechanical applications, in which large deformations are observed. Moreover, these strains are relatively low considering that, contrarily to commonly adopted DIC strain calculation schemes, no kinds of filtering and smoothing were applied to the raw data.

The MultiDIC toolbox and camera rig were utilized for in-vivo measurements to further to

illustrate the system's capabilities in clinical settings. It was shown that the dynamic full surface of the shank segment of a human subject can be reconstructed, and that a smooth strain field can be realized from the raw data. The results in Fig. 8 illustrate how the subject's lower limb shape changes due to the contraction of the calf muscles and the ankle joint angle change. This test was a proof of principle, and was not intended to provide any physiological or biomechanical finding.

The main limitation in this study is that the metrological performance tests were performed with very low-cost cameras. Therefore, the accuracies reported here are adequate only for certain applications. However, the entire procedure is expected to outperform when high quality cameras and lenses are used. The use of low-cost hardware was motivated by the large number of cameras required, and was encouraged by previous studies which demonstrated the feasibility of using consumer-grade cameras using proper distortion correction and compensation methods[33,53]. Future research could determine the performance of MultiDIC using high quality optics. Another limitation is that this study reports only on specific multi-view setup and calibration object. However, the toolbox can be easily adapted to any multi-view setup, as long as a suitable calibration object can be used.

It is noted that numerous additional algorithms for 3D-DIC exist[12,15,27,33,34,46,52], some of them offer significant advances. Moreover, an increasing number of DIC-related open source tools is seen lately[5,10,34,44,49]. In order to make these techniques more accessible and the results more reproducible, researchers are encouraged to extend the toolbox's functionality by implementing additional algorithms as contributors[9,35].

Future research by the authors will incorporate the tools established here in clinical studies, whereby the dynamic shapes of the residual limbs of lower-limb amputees will inform the mechanical design of subject-specific optimized prosthetic sockets [26]. Moreover, the subject-specific soft-tissue mechanical properties will be estimated in-vivo, by analyzing simultaneous force/torque measurements and surface deformation measurements of the entire residual limb during indentation. Then, the hyper-elastic and visco-elastic properties will be characterized using inverse finite element analysis[25,40].

CONCLUSION

This paper presents a MATLAB toolbox for 3D-DIC, which implements algorithms specifically tailored for multi-camera applications, which are often desirable in biomechanics. Several verification tests have confirmed that the MultiDIC provides accurate results using the newly developed open source software and very low-cost hardware. The development of a user-friendly, high-quality and freely available software, will greatly increase the availability of 3D-DIC to the scientific community. The capabilities to efficiently measure in-vivo skin shape and deformation were demonstrated, and future research will utilize these methods in various biomechanical studies.

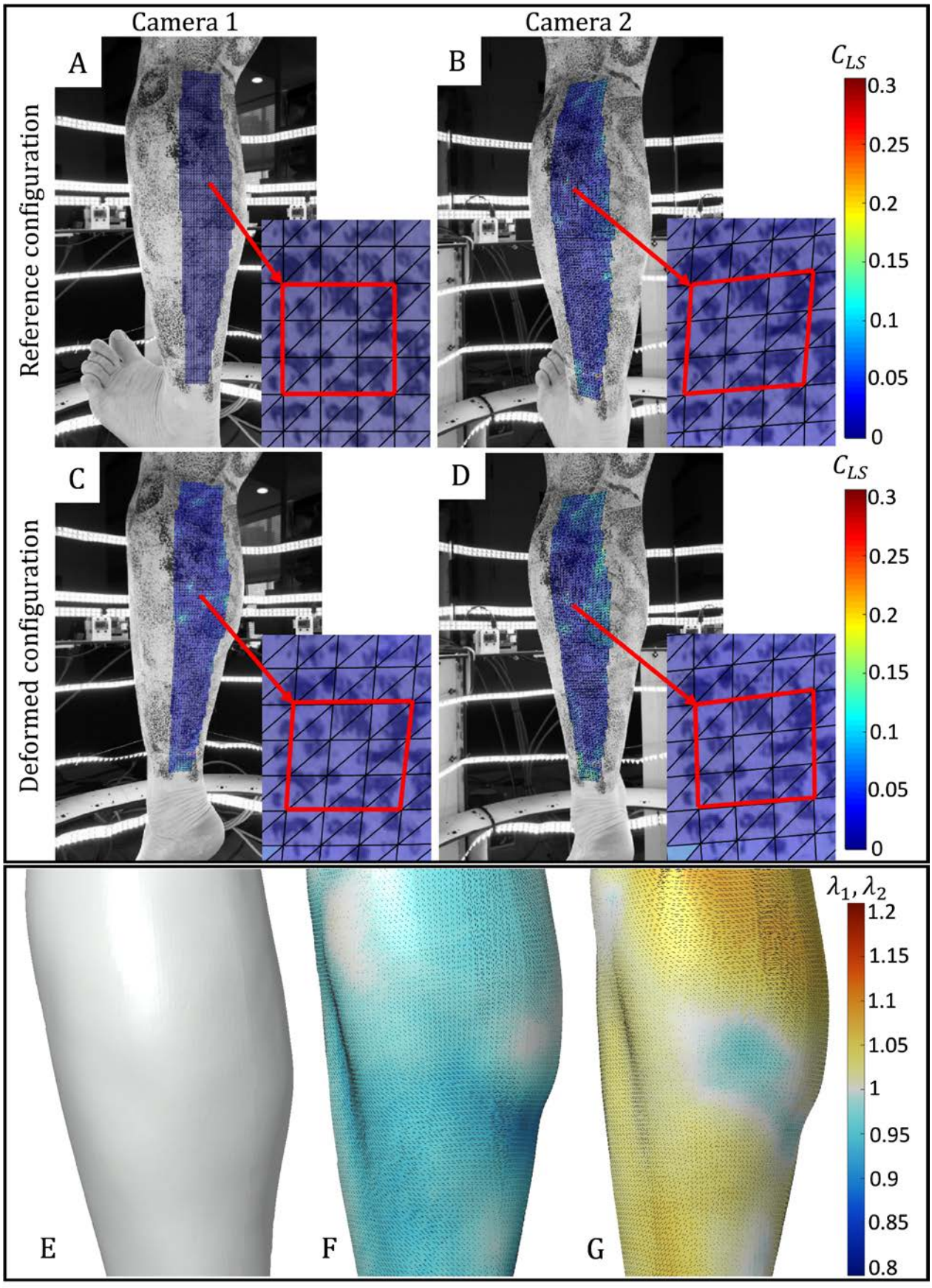
Camera 1
Camera 2
A
B
C
D
E
F
G
Reference configuration
Deformed configuration
C_{LS}
0.3
0.25
0.2
0.15
0.1
0.05
0
λ_1, λ_2
1.2
1.15
1.1
1.05
1
0.95
0.9
0.85
0.8

Fig. 8. In-vivo 3D-DIC test of a human shank. Images A-D show images from adjacent cameras in the reference (A,B) and deformed (C,D) configurations. The ROI is plotted with colors depicting the correlation coefficient, and zoomed-in portions are enlarged in insets. (E-G) The full reconstructed surface in the reference (E) and deformed (F,G) configurations. The face colors depict the principal stretch values λ_1 (F) and λ_2 (G) and the black lines represent the directions $\boldsymbol{N}_1$ (F) and $\boldsymbol{N}_2$ (G). Lighting was added to better visualize the surface contours.

APPENDIX

Appendix A: Calculation of deformations and strains

For each triangular element and for each configuration, the deformation gradient tensor $\boldsymbol{F}$ is calculated using a variation of the Triangular Cosserat Point Element (TCPE) method[41,43]. Assuming a homogenous deformation field within each element, this method obtains the finite deformation field with the same spatial resolution as the DIC measurement, and independently from adjacent data points and numerical derivatives.

The reference configuration of a given triangular face is denoted by the position vectors $\{\boldsymbol{P}_1, \boldsymbol{P}_2, \boldsymbol{P}_3\}$ of its three vertices, and the values of these position vectors in a current configuration are denoted by $\{\boldsymbol{p}_1, \boldsymbol{p}_2, \boldsymbol{p}_3\}$. Moreover, the reference and current configurations are characterized by the director vectors $\{\boldsymbol{D}_1, \boldsymbol{D}_2, \boldsymbol{D}_3\}$ and $\{\boldsymbol{d}_1, \boldsymbol{d}_2, \boldsymbol{d}_3\}$, respectively, defined as

$$\boldsymbol{D}_1 = \boldsymbol{P}_2 - \boldsymbol{P}_1;\ \ \boldsymbol{D}_2 = \boldsymbol{P}_3 - \boldsymbol{P}_1;\ \ \boldsymbol{D}_3 = \frac{\boldsymbol{D}_1 \times \boldsymbol{D}_2}{|\boldsymbol{D}_1 \times \boldsymbol{D}_2|} \tag{10a}$$

$$\boldsymbol{d}_1 = \boldsymbol{p}_2 - \boldsymbol{p}_1;\ \ \boldsymbol{d}_2 = \boldsymbol{p}_3 - \boldsymbol{p}_1;\ \boldsymbol{d}_3 = \frac{\boldsymbol{d}_1 \times \boldsymbol{d}_2}{|\boldsymbol{d}_1 \times \boldsymbol{d}_2|} \tag{10b}$$

$$\boldsymbol{D}_1 \times \boldsymbol{D}_2 \cdot \boldsymbol{D}_3 = 2A\,, \tag{10c}$$

such that $\boldsymbol{D}_3$ and $\boldsymbol{d}_3$ are unit vectors normal to the plane of the triangle in its reference and current configurations, respectively, and A is the triangle's reference area. Then, the reference reciprocal vectors $\{\boldsymbol{D}^1, \boldsymbol{D}^2, \boldsymbol{D}^3\}$ are defined by

$$\boldsymbol{D}^1 = \frac{\boldsymbol{D}_2 \times \boldsymbol{D}_3}{2A};\ \ \boldsymbol{D}^2 = \frac{\boldsymbol{D}_3 \times \boldsymbol{D}_1}{2A};\ \ \boldsymbol{D}^2 = \frac{\boldsymbol{D}_1 \times \boldsymbol{D}_2}{2A} = \boldsymbol{D}_3\,, \tag{11}$$

such that

$$\boldsymbol{D}^i \cdot \boldsymbol{D}_j = \delta^i_j\,, \tag{12}$$

where δ^i_j is is the Kronecker delta symbol. Consequently, the deformation gradient tensor $\boldsymbol{F}$ is defined by

$$\boldsymbol{F} = \sum_{i=1}^{3} \boldsymbol{d}_i \otimes \boldsymbol{D}^i, \tag{13}$$

where $\otimes$ is the tensor product (outer product) operator. $\boldsymbol{F}$ transforms any material line in the triangular element from the reference to the current configuration, including the director vectors and the principal directions, such that it satisfies

$$\boldsymbol{d}_i = \boldsymbol{F}\boldsymbol{D}_i \tag{14a}$$
$$\boldsymbol{n}_i = \boldsymbol{F}\boldsymbol{N}_i. \tag{14b}$$

Next, the right and left Cauchy-Green deformation tensors ($\boldsymbol{C}$ and $\boldsymbol{B}$, respectively), and the associated Green-Lagrangian and Eulerian-Almansi finite strain tensors ($\boldsymbol{E}$ and $\boldsymbol{e}$, respectively), are defined by

$$\boldsymbol{C} = \boldsymbol{F}^{\boldsymbol{T}}\boldsymbol{F}\ ;\ \boldsymbol{B} = \boldsymbol{F}\boldsymbol{F}^{\boldsymbol{T}} \tag{15a}$$
$$\boldsymbol{E} = \frac{1}{2}(\boldsymbol{C} - \boldsymbol{I})\ ;\ \boldsymbol{e} = \frac{1}{2}(\boldsymbol{I} - \boldsymbol{B}^{-1})\ , \tag{15b}$$

where $\boldsymbol{I}$ is the unity second order tensor. Moreover, the spectral decompositions of these tensors are given by

$$\boldsymbol{C} = \lambda_1^2(\boldsymbol{N}_1 \otimes \boldsymbol{N}_1) + \lambda_2^2(\boldsymbol{N}_2 \otimes \boldsymbol{N}_2) + \lambda_3^2(\boldsymbol{N}_3 \otimes \boldsymbol{N}_3) \tag{16a}$$
$$\boldsymbol{B} = \lambda_1^2(\boldsymbol{n}_1 \otimes \boldsymbol{n}_1) + \lambda_2^2(\boldsymbol{n}_2 \otimes \boldsymbol{n}_2) + \lambda_3^2(\boldsymbol{n}_3 \otimes \boldsymbol{n}_3) \tag{16b}$$
$$\boldsymbol{E} = E_1(\boldsymbol{N}_1 \otimes \boldsymbol{N}_1) + E_2(\boldsymbol{N}_2 \otimes \boldsymbol{N}_2) + E_3(\boldsymbol{N}_3 \otimes \boldsymbol{N}_3) \tag{16c}$$
$$\boldsymbol{e} = e_1(\boldsymbol{n}_1 \otimes \boldsymbol{n}_1) + e_2(\boldsymbol{n}_2 \otimes \boldsymbol{n}_2) + e_3(\boldsymbol{n}_3 \otimes \boldsymbol{n}_3)\ , \tag{16d}$$

where λ_i are the principal stretches, $\boldsymbol{N}_i$ and $\boldsymbol{n}_i$ are the principal directions in the reference and current configurations, and E_i and e_i are the principal Green-Lagrangian and Euler-Almansi strains, respectively. Since each triangular element is planar, one of the principal stretches must equal to one (e.g. $\lambda_3 = 1$), and one of the principal strains must equal to zero (e.g. $E_3 = e_3 = 0$). Furthermore, their associated directions are normal to the triangle's surface ($\boldsymbol{N}_3 = \boldsymbol{D}_3$ and $\boldsymbol{n}_3 = \boldsymbol{d}_3$). It is noted that although strains are more commonly presented, stretches are often preferred in large deformation cases, since their definition is unique, while numerous strain definitions besides the ones described exist (e.g. Seth-Hill class strains and Bažant strains).

Furthermore, the dilatation J, which also corresponds to the trinagle's surface area change, is given by

$$J = \det(\boldsymbol{F}) = \sqrt{\det(\boldsymbol{C})} = \lambda_1\lambda_2\ . \tag{17}$$

When the deformation is accompanied by RBM, it is often desirable to subtract the RBM such that the deformation can be visualized without significant movement of the object. Therefore, the average RBM is estimated for each configuration using the least-squares minimization approach (rigid superimposition)[39,42].

Appendix B: Camera intrinsic parameters and stereo reconstruction errors

Table 1 reports the statistics (mean ± standard deviation) of the intrinsic parameters calculated using the BA method for the twelve cameras. For each camera, 50 images were acquired of a flat checkerboard pattern with 15×20 black and white $10 \times 10\ mm^2$ squares. The number of significant digits for each parameter is based on its estimation error. The distortion parameters calculated using the original images were used for correcting the distortion on the detected image points. The corrected points were then used again for estimating the parameters. Therefore, the distortion parameters in the right column of Table 1 represent the values of the residual distortion.

Table 1. Statistics of the estimated intrinsic parameters of twelve cameras calculated using BA.

Parameter	Original image	After distortion correction
f_x	2611.7 ± 5.8	2611.9 ± 5.7
f_y	2615.4 ± 5.6	2615.7 ± 5.5
C_x	1246.5 ± 34.5	1247.7 ± 36.4
C_y	1627.7 ± 16.9	1627.2 ± 17.4
s	-1.37 ± 0.37	-1.37 ± 0.34
k_1	0.17862 ± 0.01803	0.00002 ± 0.0001
k_2	-0.295 ± 0.167	0.002 ± 0.001
k_3	-0.19 ± 0.45	0.00 ± 0.00
p_1	0.00015 ± 0.00023	0.00004 ± 0.00006
p_2	0.00068 ± 0.00066	0.00009 ± 0.00001

The reconstruction errors for the cylindrical calibration object obtained by all camera-pairs are reported in Table 2. The mean error ε_M and the root mean square error ε_R were calculated as

$$\varepsilon_M = \sqrt{\left[\sum_{n=1}^{N}\left(x_n - x_n^{(t)}\right)\right]^2 + \left[\sum_{n=1}^{N}\left(y_n - y_n^{(t)}\right)\right]^2 + \left[\sum_{n=1}^{N}\left(z_n - z_n^{(t)}\right)\right]^2} \qquad (18a)$$

$$\varepsilon_R = \sqrt{\sum_{n=1}^{N}\left(x_n - x_n^{(t)}\right)^2 + \left(y_n - y_n^{(t)}\right)^2 + \left(z_n - z_n^{(t)}\right)^2}\ , \qquad (18b)$$

where $[x_n, y_n, z_n]$ are the reconstructed point coordinates and $\left[x_n^{(t)}, y_n^{(t)}, z_n^{(t)}\right]$ are the true coordinates, and N is the number of reconstructed control points.

Table 2. Reconstruction errors for all camera-pairs.

Pair number	Camera numbers	With DC[1]		Without DC[1]	
		$\varepsilon_M[mm]$	$\varepsilon_R[mm]$	$\varepsilon_M[mm]$	$\varepsilon_R[mm]$
1	[1,2]	0.002	0.05	0.003	0.44
2	[2,3]	0.003	0.04	0.005	0.37
3	[3,4]	0.001	0.05	0.009	0.35
4	[4,5]	0.001	0.05	0.007	0.36
5	[5,6]	0.001	0.04	0.003	0.33
6	[6,7]	0.002	0.03	0.003	0.34
7	[7,8]	0.003	0.05	0.008	0.42
8	[8,9]	0.002	0.04	0.006	0.36
9	[9,10]	0.002	0.04	0.003	0.34
10	[10,11]	0.002	0.04	0.004	0.33
11	[11,12]	0.001	0.05	0.003	0.41
12	[12,1]	0.003	0.03	0.006	0.44
All cameras		0.002	0.04	0.005	0.37

[1]DC = Distortion Correction

ACKNOWLEDGMENT

This work was partially supported by the NIH grant no. 1R01EB024531-01. The work of D. Solav was partially supported by the MIT-Technion postdoctoral fellowship.

REFERENCES

1. Abdel-Aziz, Y. I. Direct linear transformation from comparator coordinates in close-range photogrammetry. , 1971.
2. Avril, S. Hyperelasticity of Soft Tissues and Related Inverse Problems. Springer, Cham, 2017, pp. 37–66.doi:10.1007/978-3-319-45071-1_2
3. Badel, P., S. Avril, S. Lessner, and M. Sutton. Mechanical identification of layer-specific properties of mouse carotid arteries using 3D-DIC and a hyperelastic anisotropic constitutive model. *Comput. Methods Biomech. Biomed. Engin.* 15:37–48, 2012.
4. Baker, S., and I. Matthews. Lucas-Kanade 20 Years On: A Unifying Framework. *Int. J. Comput. Vis.* 56:221–255, 2004.
5. Blaber, J., B. Adair, and A. Antoniou. Ncorr: Open-Source 2D Digital Image Correlation Matlab Software. *Exp. Mech.* 55:1105–1122, 2015.
6. Correlated Solutions Inc. CSI Application Note AN-722 Cylinder Data With Vic-3D <http://www.correlatedsolutions.com/supportcontent/cylinder-data-stitching.pdf>
7. Dickinson, a S., a C. Taylor, H. Ozturk, and M. Browne. Experimental validation of a finite element model of the proximal femur using digital image correlation and a composite bone model. *J. Biomech. Eng.* 133:14504, 2011.
8. Dufour, J.-E. . b, F. . Hild, and S. . Roux. Shape, displacement and mechanical properties from isogeometric multiview stereocorrelation. *J. Strain Anal. Eng. Des.* 50:470–487,

2015.
9. Erdemir, A., P. J. Hunter, G. A. Holzapfel, L. M. Loew, J. Middleton, C. R. Jacobs, P. Nithiarasu, R. Lohner, G. Wei, B. A. Winkelstein, V. H. Barocas, F. Guilak, J. Ku, J. L. Hicks, S. Delp, M. Sacks, J. A. Weiss, D. G. A. Ateshian, S. A. Maas, A. D. McCulloch, and G. C. Y. Peng. Perspectives on Sharing Models and Related Resources in Computational Biomechanics Research. *J. Biomech. Eng.* 140:24701, 2017.
10. Estrada, J. B., and C. Franck. Intuitive Interface for the Quantitative Evaluation of Speckle Patterns for Use in Digital Image and Volume Correlation Techniques. *J. Appl. Mech.* 82:95001, 2015.
11. Faugeras, O. Three-dimensional computer vision: a geometric viewpoint. 1993.
12. Gao, Y., T. Cheng, Y. Su, X. Xu, Y. Zhang, and Q. Zhang. High-efficiency and high-accuracy digital image correlation for three-dimensional measurement. *Opt. Lasers Eng.* 65:73–80, 2015.
13. Genovese, K., L. Casaletto, J. D. Humphrey, and J. Lu. Digital image correlation-based point-wise inverse characterization of heterogeneous material properties of gallbladder in vitro. *Proc. R. Soc. A Math. Phys. Eng. Sci.* 470:20140152–20140152, 2014.
14. Genovese, K., L. Cortese, M. Rossi, and D. Amodio. A 360-deg Digital Image Correlation system for materials testing. *Opt. Lasers Eng.* 82:127–134, 2016.
15. Genovese, K., and D. Sorgente. A morphing-based scheme for large deformation analysis with stereo-DIC. *Opt. Lasers Eng.* 104:159–172, 2017.
16. Heikkila, J., and O. Silven. A four-step camera calibration procedure with implicit image correction. *Proc. IEEE Comput. Soc. Conf. Comput. Vis. Pattern Recognit.* 1106–1112, 1997.doi:10.1109/CVPR.1997.609468
17. Hild, F., and S. Roux. Digital Image Correlation: from Displacement Measurement to Identification of Elastic Properties - a Review. *Strain* 42:69–80, 2006.
18. Hokka, M., N. Mirow, H. Nagel, M. Irqsusi, S. Vogt, and V.-T. Kuokkala. In-vivo deformation measurements of the human heart by 3D Digital Image Correlation. *J. Biomech.* 48:2217–2220, 2015.
19. Ito, K., K. Maeda, I. Fujiwara, K. Hosoda, T. Nagura, T. Lee, and N. Ogihara. Dynamic measurement of surface strain distribution on the foot during walking. *J. Mech. Behav. Biomed. Mater.* 69:249–256, 2017.
20. Ke, X. D., H. W. Schreier, M. A. Sutton, and Y. Q. Wang. Error Assessment in Stereo-based Deformation Measurements. Part II: Experimental Validation of Uncertainty and Bias Estimates. *Exp. Mech.* 51:423–441, 2011.
21. Lu, H., and P. D. Cary. Deformation measurements by digital image correlation: Implementation of a second-order displacement gradient. *Exp. Mech.* 40:393–400, 2000.
22. Maiti, R., L.-C. Gerhardt, Z. S. Lee, R. A. Byers, D. Woods, J. A. Sanz-Herrera, S. E. Franklin, R. Lewis, S. J. Matcher, and M. J. Carre. In vivo measurement of skin surface strain and sub-surface layer deformation induced by natural tissue stretching. *J. Mech. Behav. Biomed. Mater.* 62:556–569, 2016.
23. Malesa, M., K. Malowany, J. Pawlicki, M. Kujawinska, P. Skrzypczak, A. Piekarczuk, T. Lusa, and A. Zagorski. Non-destructive testing of industrial structures with the use of multi-camera Digital Image Correlation method. *Eng. Fail. Anal.* 69:122–134, 2016.
24. Moerman, K. M. GIBBON: The Geometry and Image-Based Bioengineering add-On. *J.*

Open Source Softw. 3:506, 2018.
25. Moerman, K. M., C. A. Holt, S. L. Evans, and C. K. Simms. Digital image correlation and finite element modelling as a method to determine mechanical properties of human soft tissue in vivo. *J. Biomech.* 42:1150–1153, 2009.
26. Moerman, K. M., D. Sengeh, and H. Herr. Automated and Data-driven Computational Design of Patient-Specific Biomechanical Interfaces. , 2016.doi:10.17605/OSF.IO/G8H9N
27. Nguyen, H., H. Kieu, Z. Wang, and H. N. D. Le. Three-dimensional facial digitization using advanced digital image correlation. *Appl. Opt.* 57:2188, 2018.
28. Obropta, E. W., and D. J. Newman. Skin strain fields at the shoulder joint for mechanical counter pressure space suit development. *IEEE Aerosp. Conf. Proc.* 2016–June:1–9, 2016.
29. Orteu, J.-J., F. Bugarin, J. Harvent, L. Robert, and V. Velay. Multiple-Camera Instrumentation of a Single Point Incremental Forming Process Pilot for Shape and 3D Displacement Measurements: Methodology and Results. *Exp. Mech.* 51:625–639, 2011.
30. Palanca, M., G. Tozzi, and L. Cristofolini. The use of digital image correlation in the biomechanical area: a review. *Int. Biomech.* 3:1–21, 2016.
31. Pan, B. Reliability-guided digital image correlation for image deformation measurement. *Appl. Opt.* 48:1535, 2009.
32. Pan, B., K. Qian, H. Xie, and A. Asundi. Two-dimensional digital image correlation for in-plane displacement and strain measurement: a review. *Meas. Sci. Technol.* 20:62001, 2009.
33. Pan, B., L. Yu, and D. Wu. High-accuracy 2D digital image correlation measurements using low-cost imaging lenses: implementation of a generalized compensation method. *Meas. Sci. Technol.* 25:25001, 2014.
34. Patel, A. K. L. M., and D. L. H. C. Franck. A q-Factor-Based Digital Image Correlation Algorithm (qDIC) for Resolving Finite Deformations with Degenerate Speckle Patterns. *Exp. Mech.* 1–16, 2018.doi:10.1007/s11340-018-0377-4
35. Peng, R. D. Reproducible research in computational science. *Science* 334:1226–7, 2011.
36. Reu, P. Virtual Strain Gage Size Study. *Exp. Tech.* 39:1–3, 2015.
37. Reu, P. L. A Study of the Influence of Calibration Uncertainty on the Global Uncertainty for Digital Image Correlation Using a Monte Carlo Approach. *Exp. Mech.* 53:1661–1680, 2013.
38. Reu, P. L., E. Toussaint, E. Jones, H. A. Bruck, M. Iadicola, R. Balcaen, D. Z. Turner, T. Siebert, P. Lava, and M. Simonsen. DIC Challenge: Developing Images and Guidelines for Evaluating Accuracy and Resolution of 2D Analyses. *Exp. Mech.* , 2017.doi:10.1007/s11340-017-0349-0
39. Rubin, M. B., and D. Solav. Unphysical properties of the rotation tensor estimated by least squares optimization with specific application to biomechanics. *Int. J. Eng. Sci.* 103:11–18, 2016.
40. Sengeh, D. M., K. M. Moerman, A. Petron, and H. M. Herr. Multi-material 3-D viscoelastic model of a transtibial residuum from in-vivo indentation and MRI data. *J. Mech. Behav. Biomed. Mater.* 59:379–392, 2016.
41. Solav, D., H. Meric, M. B. Rubin, D. Pradon, F. Lofaso, and A. Wolf. Chest Wall Kinematics Using Triangular Cosserat Point Elements in Healthy and Neuromuscular Subjects. *Ann. Biomed. Eng.* 45:1963–1973, 2017.

42. Solav, D., M. B. B. Rubin, and A. Wolf. Soft Tissue Artifact compensation using Triangular Cosserat Point Elements (TCPEs). *Int. J. Eng. Sci.* 85:1–9, 2014.
43. Solav, D., M. B. Rubin, A. Cereatti, V. Camomilla, and A. Wolf. Bone Pose Estimation in the Presence of Soft Tissue Artifact Using Triangular Cosserat Point Elements. *Ann. Biomed. Eng.* 44:1181–1190, 2016.
44. Sur, F., B. Blaysat, and M. Grédiac. Rendering Deformed Speckle Images with a Boolean Model. *J. Math. Imaging Vis.* 1–17, 2017.doi:10.1007/s10851-017-0779-4
45. Sutton, M. A., and F. Hild. Recent Advances and Perspectives in Digital Image Correlation. *Exp. Mech.* 55:1–8, 2015.
46. Sutton, M. A., F. Matta, D. Rizos, R. Ghorbani, S. Rajan, D. H. Mollenhauer, H. W. Schreier, and A. O. Lasprilla. Recent Progress in Digital Image Correlation: Background and Developments since the 2013 W M Murray Lecture. *Exp. Mech.* 57:1–30, 2017.
47. Sutton, M. A., J.-J. Orteu, and H. Schreier. Image Correlation for Shape, Motion and Deformation Measurements. Boston, MA: Springer US, 2009.doi:10.1007/978-0-387-78747-3
48. Triggs, B., P. F. McLauchlan, R. I. Hartley, and A. W. Fitzgibbon. Bundle Adjustment — A Modern Synthesis. Springer, Berlin, Heidelberg, 2000, pp. 298–372.doi:10.1007/3-540-44480-7_21
49. Turner, D. Digital Image Correlation Engine (DICe) Reference Manual. , 2015.
50. Wang, Y., P. Lava, S. Coppieters, P. V. Houtte, and D. Debruyne. Application of a multi-camera stereo DIC set-up to assess strain fields in an Erichsen test: Methodology and validation. *Strain* 49:190–198, 2013.
51. Wang, Y. Q., M. A. Sutton, X. D. Ke, H. W. Schreier, P. L. Reu, and T. J. Miller. On Error Assessment in Stereo-based Deformation Measurements. *Exp. Mech.* 51:405–422, 2011.
52. Wittevrongel, L., P. Lava, S. V. Lomov, and D. Debruyne. A Self Adaptive Global Digital Image Correlation Algorithm. *Exp. Mech.* 55:361–378, 2015.
53. Yu, L., and B. Pan. In-plane displacement and strain measurements using a camera phone and digital image correlation. *Opt. Eng.* 53:54107, 2014.
54. What Is Camera Calibration? - MATLAB & Simulink <https://www.mathworks.com/help/vision/ug/camera-calibration.html>